https://doi.org/10.5194/egusphere-2025-672
Preprint. Discussion started: 24 February 2025

Detection of Multi-Modal Doppler Spectra. Part 2: Evaluation of the Detection Algorithm and Exploring Characteristics of Multi-modal Spectra Using a Long-term Dataset

Sarah Wugofski[1], Matthew R. Kumjian[1]

[1]Department of Meteorology & Atmospheric Science, The Pennsylvania State University, University Park, Pennsylvania, USA

Correspondence to: Sarah Wugofski (sjw5417@psu.edu)

Abstract.

In this paper, we process three years of vertically pointing Ka-band radar spectral data according to the methodology described and established in Part 1 (Wugofski et al. 2025). Across three years of data, we demonstrate the detection algorithm is successful in identifying multi-modal spectra, with 90.8% of detected events verifying. Beyond the verification, we explore other characteristics of the detected events such as the height, depth, and temperature of the layers containing secondary modes. Reanalysis data from ERA-5 was used to gain additional context to the environmental conditions associated with the detected events. By connecting temperatures from ERA-5 with the detected layers, we access the potential for these events to be associated with common microphysical processes such as growth of columns or plates, Hallett-Mossop rime splintering, dendritic growth, and primary ice nucleation. We further explore the potential microphysical processes revealed by the multi-modal spectra using linear depolarization ratio to determine if the secondary mode may comprise ice crystals that can produce such a signal. Of the cases with a detected enhanced LDR signal, >55% of those occurred in a layer with a mean temperature consistent with Hallett-Mossop rime splintering. Finally, three cases are investigated in more detail to illustrate the variety of events detected by the algorithm.

1 Introduction and Background

Remote sensing observations of cloud and precipitation, such as those from polarimetric radar, are useful in determining particle properties including size, aspect ratio, depolarization characteristics, and concentrations through variables such as reflectivity (Z), differential reflectivity (Z_{DR}), linear depolarization ratio (LDR), and specific differential phase (K_{DP}). In particular, exploring vertical changes in radar measurements – coined “fingerprints” (Kumjian et al., 2022) – provides information about changes to precipitation particles as they descend to the surface. When using vertically pointing radar, the mean Doppler velocity observation (MDV) can inform on particle fall speeds, vertical air motion, and/or the presence of turbulence and spectrum width (SW) can inform on the spread of MDV (see Part 1 and references therein). One of the most useful products from a vertically pointing radar is the Doppler spectrum, which can used for examining microphysical processes, including those with multiple types of hydrometeors are present. Doppler spectra, often visualized through spectrogram plots, show the distribution of returned power (or Z) across a range of Doppler velocities that can be often considered a proxy for particle fall speeds. Because different types of cloud and precipitation particles have varied sizes and masses, they have different fall speeds (e.g., Lamb and Verlinde, 2011), and thus their contributions to the Doppler spectrum often can be distinguished.

Spectral data contain particularly rich information for mixed-phase clouds, where particles such as cloud droplets, drizzle, ice crystals, and snow aggregates may coexist in the same radar sampling volume. Mixed-phase cloud processes are of particular interest because, for example, in the Arctic, mixed-phase clouds are long lived and cover large areas (e.g., Shupe et al., 2011; Morrison et al., 2012), and thus have a large impact on radiative fluxes, which has implications to understanding climate impacts (Shupe and Intrieri, 2004; Zuidema et al., 2005; Morrison et al., 2012). Mixed-phase processes involve both liquid and ice hydrometeors, and can also include certain secondary ice-production mechanisms like Hallett-Mossop rime splintering (Hallett and Mossop, 1974) and droplet shattering (Field et al., 2017). These processes remain a great source of uncertainty in how we understand and represent the generation of ice particles, and so further investigations are needed (Field et al. 2017; Korolev et al. 2017). These processes can be investigated using radar Doppler spectra, particularly cases with multi-modal Doppler spectra (Luke et al., 2021; Billault-Roux et al., 2023).

In Part I, we show that multi-modal Doppler spectra from vertically pointing radars have a distinctive combination of large values of mean spectrum width ($\overline{SW}$) and small values of the standard deviation of mean Doppler velocity ($\sigma(MDV)$) over short (145-s long) data segments. In combination, these two quantities can be used to identify multi-modal layers, which were found to fall within a separate area of the $\overline{SW}$- $\sigma(MDV)$ parameter space compared to turbulent layers and non-turbulent, single-modal layers. An algorithm to detect the combination of these two quantities in vertically pointing radar moment data was created. Having established a proposed methodology for the detection of multi-modal spectra through radar moment processing, the algorithm can now be assessed for its ability to detect these events.

Here, we seek to evaluate the method proposed in Part 1 to identify multi-modal spectra events through analysis of radar moment variables. We test this algorithm using three years of data collected at the U.S. Department of Energy (DOE) Atmospheric Radiation Measurement (ARM) program North Slope of Alaska (NSA) site, and statistically evaluate its performance based on manual verification. We can then examine the temperatures associated with detected multi-modal spectra and determine potential microphysical processes associated with the detected events. Although radar observations alone often are insufficient to conclude with certainty what processes are active in generating and growing observed hydrometeors, through observations of their fall speeds, depolarization signals, and proximal temperature profiles, we can assess how commonly the conditions favorable for such processes occur within this dataset.

2 Data and Methods

2.1 Radar and Algorithm

We apply the criteria established in Part 1 to three years of data collected by the NSA Ka-band ARM Zenith-pointing Radar (KAZR; see Part 1 for specifications). Specifically, we use the years 2020, 2022, and 2023. (Note that NSA KAZR data from

2013 were used in the development of the criteria, so we chose independent years on which to perform the evaluation.) Further, there were changes in data formatting in 2019; the CfRadial data format was adapted partway through 2019 and is currently used for KAZR data (Toto and Giangrande, 2019-2023; Feng et al., 2019-2023). For consistency, we use years after the change to the CfRadial convention. There is a significant gap in reliable KAZR spectra data in 2021 (March through October), in which data were negatively affected by artificial spectral broadening. The artificial broadening was likely caused by a malfunctioning phase lock oscillator that was ultimately replaced on 19 October 2021 (Min Deng, 2024, personal communication). Thus, 2021 is omitted from our analysis.

To process the long-term KAZR dataset, we partition the data into 145-s segments, matching those used for the algorithm development (Wugofski et al., 2025; hereafter Part 1). We keep the data segments a consistent duration because parameters (including the standard deviation) can change with increasing data temporal length. For each of these 145-s segments, we create vertical profiles of spectrum width (SW), mean Doppler velocity (MDV), signal-to-noise ratio (SNR), and linear depolarization ratio (LDR) with 30-m vertical resolution (matching the vertical resolution of KAZR). Points with a $\overline{SW} > 0.19$ m s^{-1} and $\sigma(MDV) < 0.1$ m s^{-1} are flagged for being a potential secondary mode. Additionally, a SNR criterion is applied to filter out noise: data with SNR < -5 dB are omitted. Further, data with MDV < -2 m s^{-1} are excluded, because such large implied fallspeeds are suggestive of being from rain (see Part 1 for details).

Results of the detection algorithm (i.e., the “flagged” points) are then consolidated into detected cases. We set a minimum case duration of two hours to focus on persistent secondary mode signals. When examining the detected (“flagged”) points in time-height space, we find they generally cluster into layers or streak-like features (Fig. 1). Whereas layers have a relatively constant height over time, streaks have a decreasing height over time. In some instances, there is speckling of flags that do not form a cohesive feature (e.g., as seen between 0-1 km and 4-5 km in Fig. 1b). The threshold for defining a case is set at 100 flags per hour, sustained for two hours. Several factors contributed to the choice of 100 flags hr^{-1} as the threshold: with the 145-s and 30-m resolution of the NSA KAZR data, it takes approximately 100 flags to capture 15 minutes of a 0.5-km-deep multi-modal layer. Additionally, after examining the hourly flag results, we observed sustained periods exceeding 100-200 flags hr^{-1}, which will be further discussed in the results. In few cases, hourly flag counts were interrupted by an hour with >90 but <100 flags; to avoid artificially inflating the case count, we consolidate these situations into a single case.

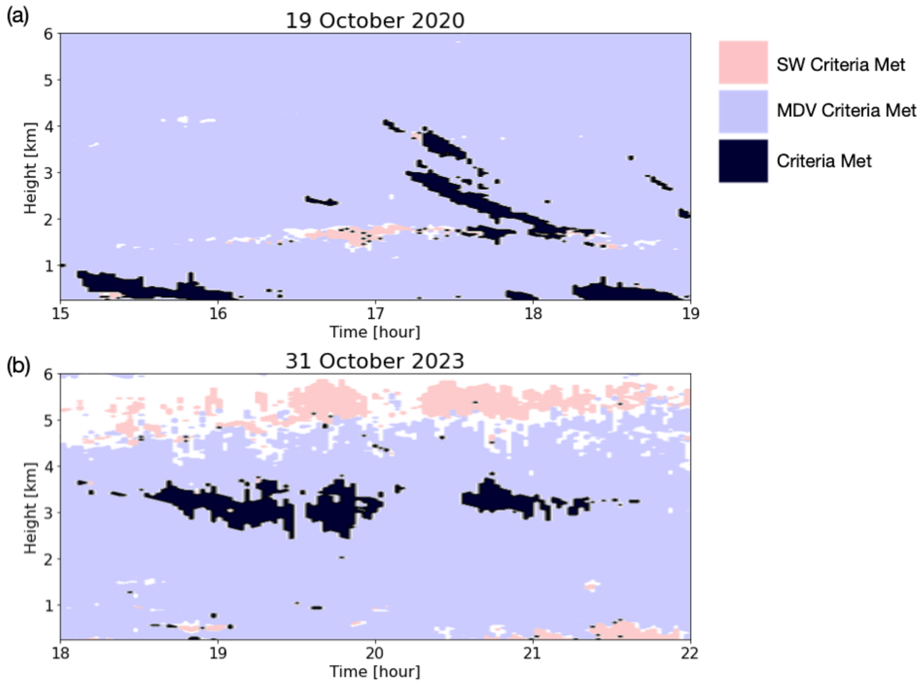

Figure 1: Time-height depiction of radar gates that met the SW criterion (pink shading), the MDV criterion (blue shading), and where both criteria are met (black shading), indicating regions containing flags identified through the multi-modal detection algorithm. (a) On 19 October 2020 the flags presented in streaks, beginning at higher altitude and dissipating at lower altitudes. (b) On 31 October 2024 the flags persisted in a layer.

The detected cases are then manually verified through examination of instantaneous radar spectra, produced for every five minutes of a case. The secondary mode must be distinctly separated from the primary mode for the case to verify; we required at least a 5-dB decrease between the primary and secondary modes' peak values (see Part 1). During this step, the spectra are also checked for possible false detections due to turbulence or broadening from melting. In this way, we can compute the verification rate for the detection algorithm, as well as the false detection rate. (We cannot assess missed detections without manual examination of the entire three-year dataset, which is unreasonably time consuming.)

2.2 ERA-5

To better understand the forcings and processes associated with detected multi-modal events, ERA-5 reanalysis (Hersbach et al., 2019) data complement the algorithm results and observed radar signals. Although there are upper-air observations from radiosondes taken at the NSA site, they are only available routinely twice daily, and thus often not occurring at the same time as the detected cases. The ERA-5 reanalysis provides a long-term dataset of kinematic and thermodynamic variables to better understand how they may relate to detected multi-modal spectra cases. Specifically, we consider ERA-5 monthly mean pressure-level data. We examine the Pearson correlation coefficient between flag count and several dynamic, thermodynamic, and microphysical variables at model levels ranging from 1000 to 200 hPa. These correlations are computed for the entire dataset and on an annual basis. Several months in 2022 had incomplete KAZR data from periods in which the radar was not operational. To avoid correlations being affected by incomplete data, months with >10 missing days are neglected from the ERA-5 analysis; this includes July-September of 2022.

For the detailed case analyses, we use the ERA-5 hourly pressure-level data to extract thermodynamic information from a 1º x 1º box surrounding the NSA site (71.323º, -156.615º) for every other hour during the case. Data from within the box are averaged, and then we interpolate the vertical profiles from the 23 pressure levels to 90 height levels extending from 0 to 8.9 km in 100-m increments.

3 Results

3.1 Case Verification

The algorithm results can be examined in two frameworks: flag occurrence and case occurrence. We first discuss the cases. In considering the case counts, note that both 2022 and 2023 are influenced by periods of missing data. In 2022 there are short periods of missing data periodically from June through November of 2022 that may affect the total case counts in those months; these months contain 13-26 days rather than the expected 30-31. In July 2023, KAZR moment data was available but spectra were unavailable from 2-23 July. Across the three analysis years, 184 cases were found across 144 dates (Table 1). Of those cases, 90.8% (167) were verified by manual review of the Doppler spectra to have a secondary mode separated by local minimum in spectral power of >5 dB below the peaks. The verification rate was consistent across the three years, ranging from 88.9% to 91.4% (Table 1). The fewest cases were identified in 2022, with only 40 verified out of 45 total cases. 2020 and 2023 saw 70 and 69 cases, respectively, with both years only having six cases that did not verify. Nonverifying cases have a separation of less than 5 dB between modes (i.e., they were less distinct but still multi-modal) or symmetric broadening of a single mode.

On average, 15.5 cases were detected per month, with 13.9 of those verifying as having secondary modes. When looking at all three years in aggregate, the months with the most identified cases are August, September, and October (Fig. 2). While seasonal trends appear in this data, they are affected by the periods of missing data in 2022-2023 mentioned previously. Despite the missing data, when considering the seasonal pattern extending from June through October, the NSA warm season sees a greater number of detected multi-modal spectra cases. Note that, particularly in the warmer months, an MDV threshold was used to filter out any spectral broadening associated with large drizzle and/or rain, so the detected warm season cases are occurring above the melting layer.

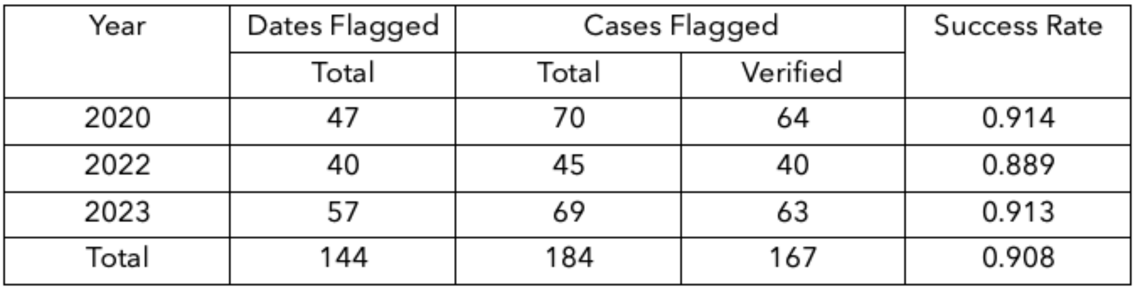

Year	Dates Flagged	Cases Flagged		Success Rate
	Total	Total	Verified	
2020	47	70	64	0.914
2022	40	45	40	0.889
2023	57	69	63	0.913
Total	144	184	167	0.908

Table 1: Total number of dates flagged, total number of cases flagged and verified, and the algorithm success rate (correct detections, expressed as a fraction), by year and total across the 3-year period.

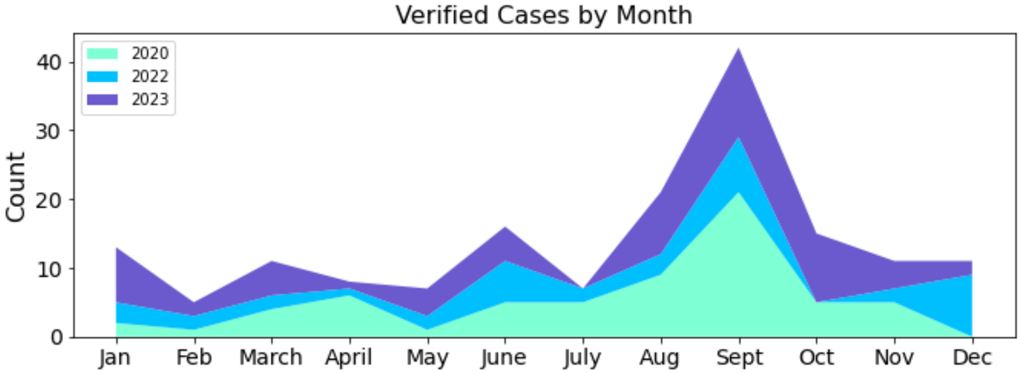

Figure 2: Count of the number of verified cases by month, colored by year. 2020 is light green, 2022 is blue, and 2023 is purple.

The median case length is 3 hr in duration (Fig. 3a); recall there is an imposed cut-off at two hours by the definition of a case set forth in the methodology (any single-hour cases have been excluded). The mean case duration is approximately 4 hours. These durations are suggestive of the timescales involved in the microphysical processes leading to the observed multi-modal spectra. The large frequency of occurrence of 2-4 hour multi-modal events, compared to sustained 5+ hour events, suggests that they are the result of processes that occur on shorter time scales. Despite the vast majority of cases having durations < 6 hr, longer cases are present throughout the dataset. Examining cases lasting > 6 hr reveals they are more common in August and September (not shown, discussed more in 3.2). These long-lived cases generally occur in the months with the most verified cases. Only 5% of verified cases last >10 hr, and the maximum duration observed was 17 hr.

To investigate the case layer heights and depths, we use the 25th and 75th percentiles of flag heights to delineate the layer for each day. These are then investigated for dates that have verified cases. Detected multi-modal layers are present exclusively within the lower 4 km (Fig. 3b). The mean height at which these layers are detected is between 1.5 and 2 km. The depth of detected multi-modal layers is quite variable: the mean and median layer depths are 1.23 km and 1.06 km, respectively. Half of the verified multi-modal layers were shallower than 1 km, suggesting that processes creating and sustaining secondary modes are operating at a similar or shallower depth. Deeper layers are moderately correlated (Pearson correlation coefficient *r* = 0.55) with higher mean layer heights. Less than 16% of depths were >2 km; these deeper layers are likely explained by a combination of streak-like features that vary in height with time and dates with more than one distinct case present in a single day.

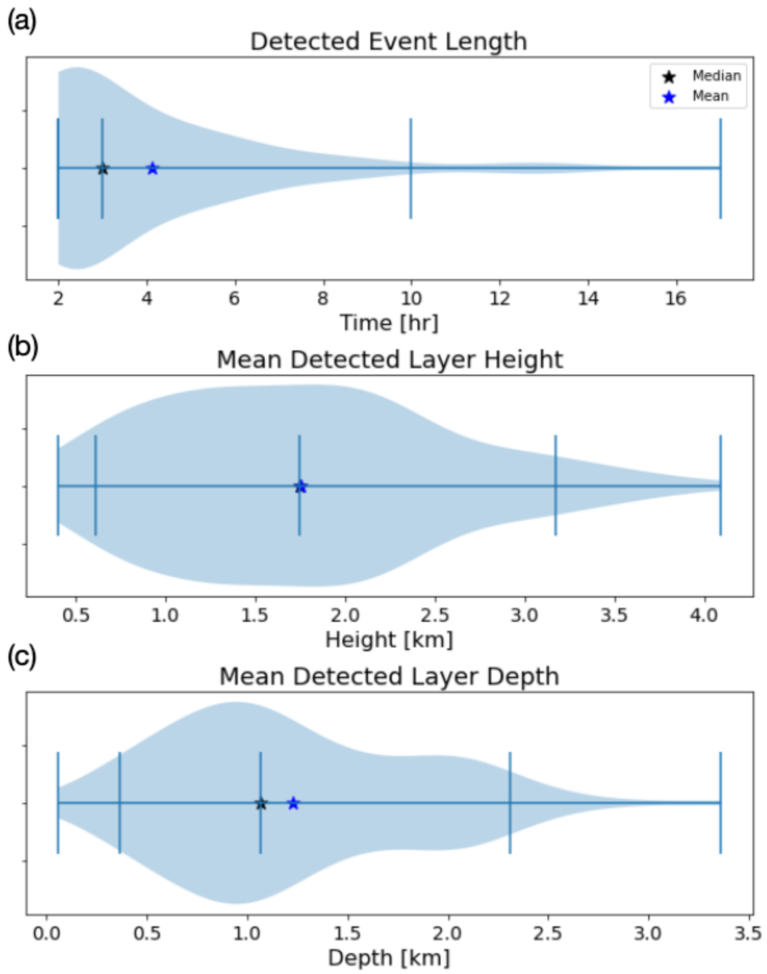

Figure 3: Violin plots showing the distributions of (a) case duration (hr), (b) mean height of the detected layer (km), and (c) mean depth of the detected layer (km). The median and mean of the distributions are marked by black and blue stars, respectively. Vertical bars represent (from left to right): the minimum, the 5th percentile, the median, the 95th percentile, and the maximum.

3.2 Flag Frequency Analysis

Examining the temporal distribution of flags across the three-year analysis period (Fig. 4 and Appendix) reveals visibly active times in which >100 flags hr^{-1} are observed for extended durations. It is common for flagged hours to be clustered together as a multi-hour event, though some instances of isolated, single-hour periods with large flag counts do occur (e.g., 27 April 2020 at 19 UTC with 406 flags, and Figure 23 May 2020 at 19 UTC with 233 flags). In contrast, there are many multi-hour sustained events apparent, such as 6-7 August 2020. This case lasted 10 hr with an average flag count of 228 flags hr^{-1}, minimum of 108 flags hr^{-1}, and a maximum of 532 flags hr^{-1}. Similarly long cases with sustained flag counts exceeding 200 hr^{-1} can be seen 15 April 2020 and throughout September 2020. While the cases with flag counts exceeding 200 hr^{-1} stand out visually in Fig. 4, sustained cases with flag counts between 100-200 hr^{-1} are also observable, such as 3 December 2020 from 10-12 UTC. The flag count for this event ranges from 95-159 hr^{-1}. These results for 2022-2023 can be found in the Appendix.

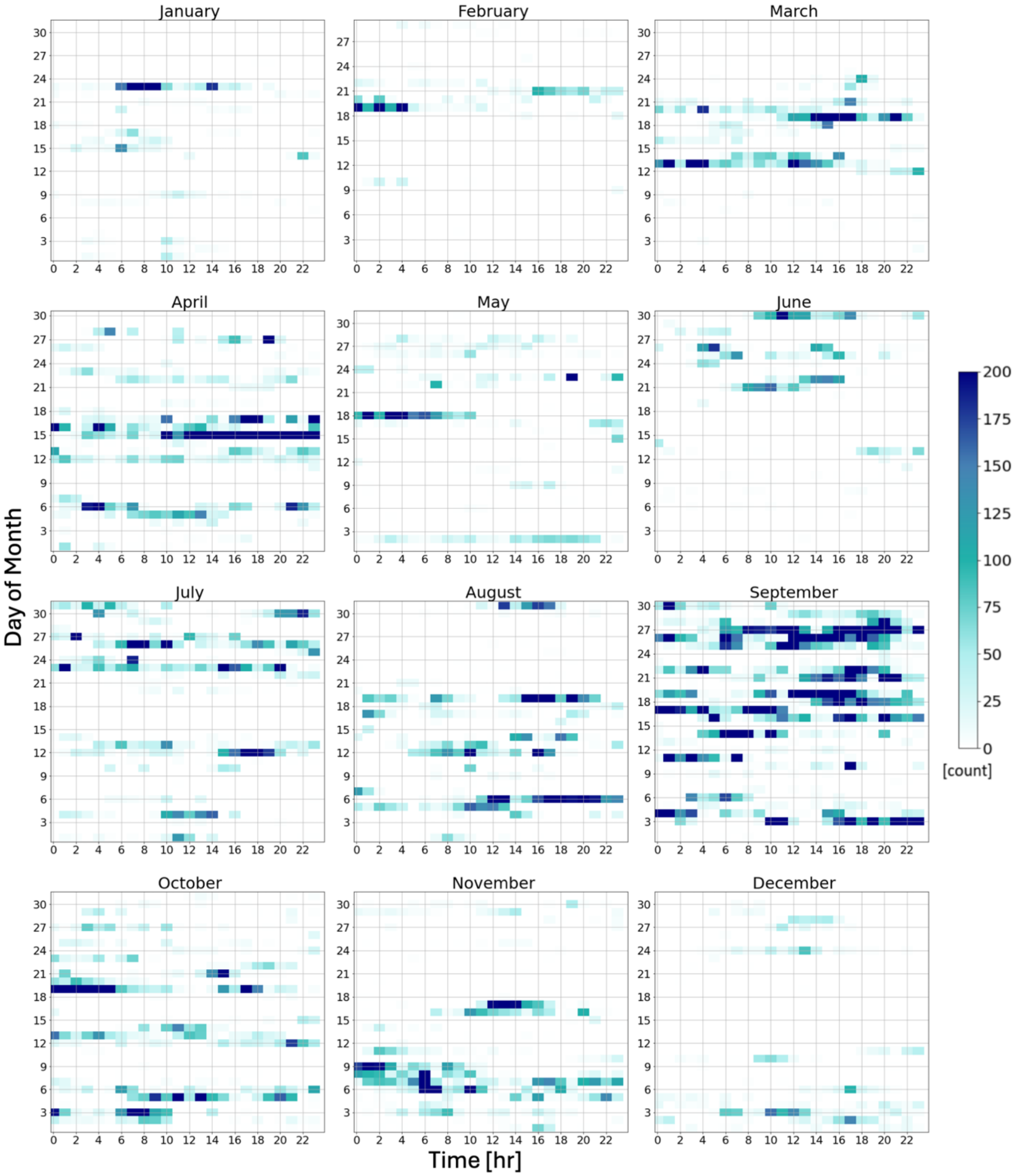

Figure 4: Hourly flag occurrence for the year 2020. On each panel, the x axis is hour UTC and the y axis is day of month. Darker shades represent more flags occurring in a given hour, according to the color bar. The years 2022 and 2023 are shown in the Appendix.

185

In examining a single year, such as 2020, visually there seems to be seasonality to detected events. This can be more fully understood by examining thermodynamic, microphysical, and kinematic quantities in conjunction with the detected events. Such an examination can be revealing because the characteristics of the flagged cases are likely governed by the microphysical processes leading to the observed multi-modal spectra, and thus, the environments supporting these processes. To determine if any seasonal trends exist that could explain detected layer properties, we compute correlations between the monthly flag count and ERA-5 monthly mean thermodynamic, kinematic, and microphysical variables at 23 pressure levels ranging from 1000 to 200 hPa (Fig. 5; 1000, 975, 950, 925, 900, 875, 850, 825, 800, 775, 750, 700, 650, 600, 550, 500, 450, 350, 300, 250, 225, 200 hPa[1]).

Between the surface and 300 hPa (i.e., covering the entire range of detected layer heights), monthly mean temperature and specific humidity both have moderate positive correlations (0.4 to 0.6) to flag counts. The positive correlation between flag count and specific humidity makes sense, given that one would expect moister months to be more likely to produce clouds (and thus microphysical processes that could generate multi-modal spectra). The positive correlation between flag count and temperature helps to explain some degree of seasonality in the flag and case distributions: many of the colder months contain fewer flags and cases than warmer months. Seasonality, however, cannot fully explain the distribution of flags and cases. Pressure vertical velocity (ω, in Pa s^{-1}) exhibits a moderate negative correlation (-0.4 to -0.6) with flag count in the layer between 850 and 400 hPa. Negative pressure vertical velocity implies upward air motion, and so the negative correlation makes sense: large-scale ascent favors cloud and precipitation development. Relative vorticity is only weakly positively correlated (<0.2) with flag count at altitudes below 500 hPa, and weakly negatively correlated (>-0.2) at heights above 500 hPa, implying a lack of any meaningful connection between flag count and synoptic-scale patterns. In its representation of microphysics, ERA-5 has five prognostic variables (cloud fraction, cloud ice water content, cloud liquid water content, snow water content, and rain water content; Tiedtke, 1983; Forbes et al., 2011). Because all water content is divided across those four classifications, graupel, ice pellets, and hail are not considered within the model (any rain drops that freeze are classified as snow; Forbes et al., 2011).

Unsurprisingly, fractional cloud cover has the greatest correlation with flag counts (>0.6) for the layer between 950-800 hPa. By identifying radar signals with the detection algorithm, we are detecting clouds; the moderate-to-strong correlations suggest the ERA-5 reanalysis dataset is producing cloudy conditions during the detected events. For all altitudes above 950 hPa, all water contents have positive correlations with flag count, including some (cloud liquid and snow water content) exceeding 0.6. The height at which each category has maximized correlation varies: rain water content's maximum correlation is at the surface, snow at 775 hPa, cloud liquid at 825 hPa, and cloud ice at 550 hPa. The moderately strong positive correlations of both ice and liquid may suggest that mixed-phase clouds are commonly present during detected events. However, any attribution of microphysical processes must be further pursued on a case-by-case basis to better understand these connections.

---

[1] Note that not all variables contain values above a certain pressure level, such as rain water content and snow water content. These 23 levels are all of the pressure levels available below 200 hPa.

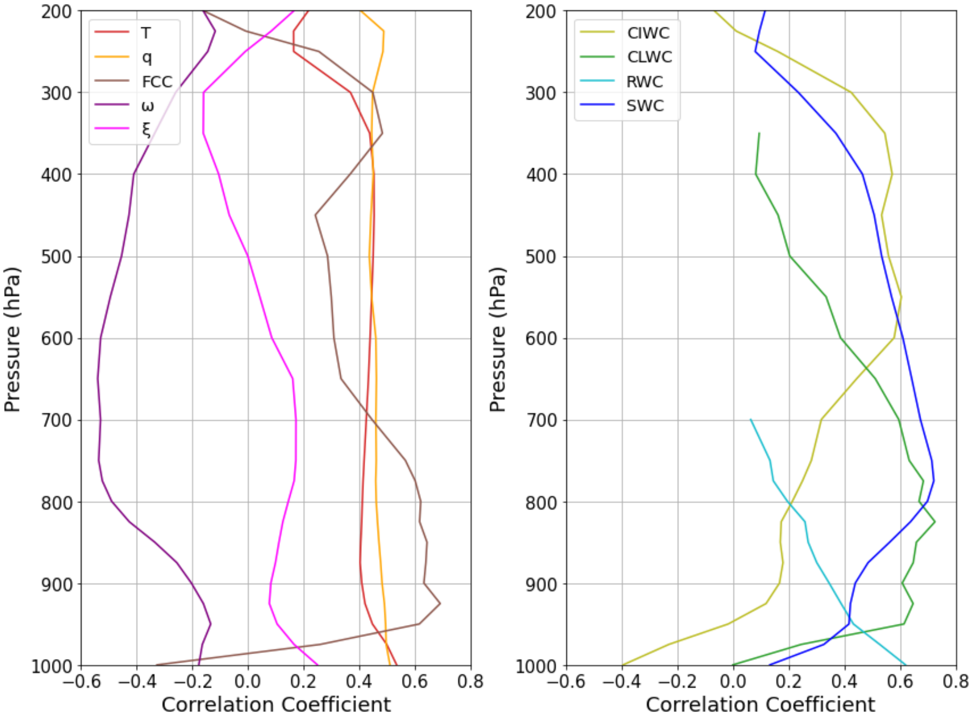

Figure 5: Vertical profiles of Pearson linear correlation coefficient between monthly flag count and (a) thermodynamic and kinematic variables: temperature (T, red), specific humidity (q, orange), fractional cloud cover (FCC, yellow), pressure vertical velocity (ω, purple), and relative vorticity (ξ , magenta), and (b) microphysical variables: cloud ice water content (CIWC, yellow-green), cloud liquid water content (CLWC, green), rain water content (RWC, teal), snow water content (SWC, blue).

4 Process Identification

Having demonstrated success in identifying multi-modal spectra through only the use of radar moment data, the next question arises: how do we determine the physical processes responsible for these features? Radar observations can provide insight into the shape, size, and concentration of hydrometeors, but ambiguity remains as to what processes are active within a cloud and responsible for the generation and growth of the observed hydrometeors.

Identifying the makeup of the primary and secondary modes is challenging. Observed modes may comprise ice or liquid; recall that these modes are distinctly separated by their fall speeds and are commonly referred to as the primary mode being the fastest falling, and the secondary/tertiary as slower-falling modes. Secondary modes can contain slow-falling ice generated from primary nucleation or secondary processes, or small liquid cloud or drizzle droplets. One important consideration is temperature: certain processes are active in specific temperature ranges such as dendritic growth from -18 to -12ºC. Secondary modes may also contain small liquid cloud or drizzle droplets (Luke et al., 2010; Verlinde et al., 2013). This distinction is commonly made using LDR (e.g., Oue et al., 2015; Sinclair et al., 2016). For vertically pointing radar, the LDR observed in columnar ice crystals is much larger than that of liquid droplets (except for melting ice hydrometeors, which can exhibit large LDR (Devisetty et al. 2019; Kumjian et al. 2020). Determining whether a mode is ice or liquid is insufficient for process determination, however. Studies of secondary ice production mechanisms consider their efficiency at various temperatures, and some have revealed rather stringent requirements. For example, Hallett-Mossop rime splintering is specific to the temperatures of -3<T<-8ºC (Hallett and Mossop 1974). To shed some light on the possible underlying physical processes responsible for the observed multi-modal spectra, we analyze both the temperatures and LDR associated with each verified case.

4.1 Temperature

To analyze the temperature profiles associated with the verified cases, we use the 25th and 75th percentile flagged heights for each hour of data of each flagged case and use the ERA-5 dataset to calculate the mean temperature and temperature range within the layer. These distributions are presented in Fig. 6. Note that the general climate of the NSA site analyzed here will affect the distribution of temperatures associated with detected multi-modal spectra events and are likely unique to the Arctic climate of NSA and not applicable to multi-modal spectra events detected in mid-latitude or other environments.

The mean temperatures are skewed towards greater values, with the upper 50% of hourly case data featuring temperatures between about –6 and +4 °C (Fig. 6a). However, the distribution features a long tail towards lower values, with some cases as cold as –28 °C. The temperature ranges associated with multi-modal layers are shown in Fig. 6b: >50% of the cases have a temperature range < 5 °C within the layer. Cases with temperature ranges >5 °C are attributable to deeper flagged layers. Manual inspection of the data revealed that some cases with fall streaks with vertical extents > 1 km are responsible for some of these larger temperature ranges.

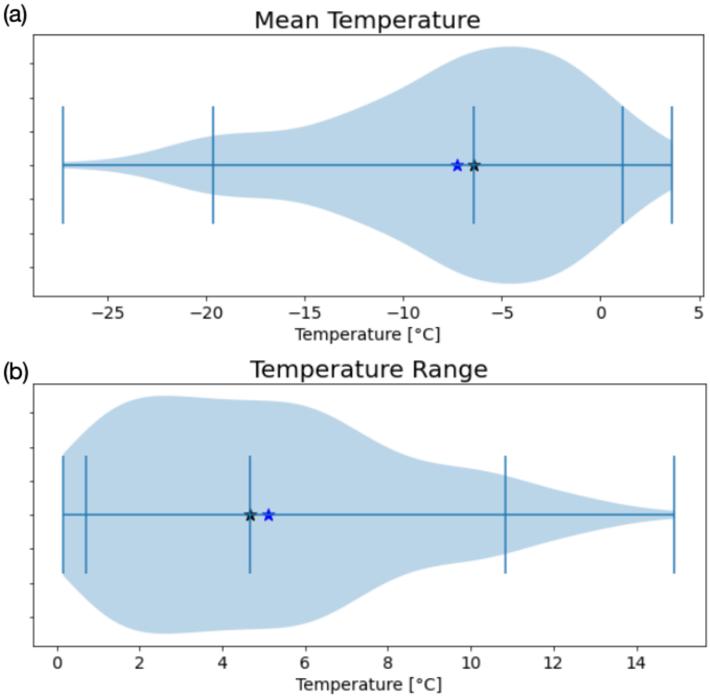

Figure 6: Violin plots showing the distributions of (a) mean temperature of the detected layer (ºC), and (b) temperature range of the detected layer (ºC). The median and mean of the distributions are marked by black and blue stars, respectively. Vertical bars represent (from left to right): the minimum, the 5th percentile, the median, the 95th percentile, and the maximum.

We can partition the case mean temperatures into categories to access the favorability of certain processes such as rime splintering and dendritic growth. The dark blue bars in Fig. 7 show the percentage of cases that fall within the prescribed temperature ranges. To focus on mixed-phase and ice processes, we exclude 9% of the total cases that have an associated mean layer temperature ≥0 °C. While the rain filter described in Part 1 and the Methods section is targeted at eliminating or reducing the detection of rain, melting and rain may be present in some of the warmer detected cases[2].

4.2 LDR

LDR is useful in distinguishing liquid from ice hydrometeors in vertically pointing radar data. The LDR moment data (i.e., integrated over the spectrum) associated with each flagged time and height is used for the analysis here. Because the moment LDR data comprise contributions from both the primary and secondary modes, LDR is not solely determined by the secondary

---

[2] Cases in the temperature distribution statistics presented in Figure 6 are verified multi-modal cases. Recall there is a criterion on MDV to exclude rain. Higher temperatures may, in part, be due to temporal or spatial displacement of the melting layer between the radar observations and modeled clouds in the reanalysis dataset.

mode. Thus, the moment LDR generally will not be as enhanced as the underlying secondary mode may be (particularly those attributable to pristine columnar ice).

Due to maintenance of KAZR in 2021, the radar's lower LDR limit is significantly different in 2022-23 compared to 2020 (personal communication, Min Deng, 2024). To identify when cases have an LDR above the system limit associated with them, we first identify the average LDR associated with all cases within each year. We then add two standard deviations (calculated from this distribution of average LDR values from each year of cases) to this average to establish what threshold value we consider to be significantly greater than the average LDR. This results in the following LDR criteria: (i) for 2020: -17.50 dB, (ii) for 2022: -21.98 dB, (iii) for 2023: -21.48 dB. To determine what cases have layers with enhanced LDR values, we determine whether the 95th percentile flagged LDR for each case exceeds these thresholds. This was tested with both the 90th and 95th percentiles, which yielded a similar number of cases. This results in 18 days in 2020, 22 days in 2022, and 25 days in 2023 with multi-modal spectra events exceeding the LDR thresholds. For days with multiple distinct cases, we examine all cases on that date. These cases are then manually verified with spectral LDR computed from the co- and cross-polar radar spectra to determine which cases have secondary modes featuring enhanced spectral LDR values consistent with ice crystals.

Combining both LDR and temperature information, we find that 93.9% of the multi-modal spectra cases with enhanced LDR occur in a layer with mean temperature > -8 °C (Fig. 7; light blue bars), a disproportionately larger fraction than for all cases. There are two factors that may explain this result: melting is associated with increased LDR, and pristine columnar ice modes are associated with increased LDR. Only 34.1% of the cases feature mean temperatures >-3 °C, suggesting that melting is not the dominant contributor to these results. Instead, 59.8% of the multi-modal spectra cases with enhanced LDR occur within the temperature zone favorable for Hallett-Mossop rime splintering (-3 to -8 °C) or primary nucleation of columnar crystals (e.g., Bailey and Hallett 2009). Only 2.44% of enhanced LDR cases occur in the colder portion of the columnar habit temperature range (-8 to -12 °C), suggesting that Hallett-Mossop rime splintering could be playing a role in this subset of the detected cases. However, we cannot rule out other secondary ice mechanisms such as droplet shattering or collisional fragmentation, or and new primary nucleation of columnar crystals (amongst extant snow and ice descending into this layer from above). In contrast, disproportionately few enhanced-LDR cases exist for temperatures lower than -12 °C, indicating that processes involving planar crystal habits or polycrystalline habits are not likely to produce secondary spectral modes with enhanced LDR values.

More confident process attribution requires a more detailed analysis of individual cases, likely along with ancillary measurements. In the next section, we examine three cases in more detail to highlight the rich diversity of multi-modal spectral cases that can be identified using our proposed detection algorithm. We will examine cases within the warm (> -3 °C), Hallett-Mossop (-3 to -8 °C), and dendritic (-12 to -18 °C) temperature zones.

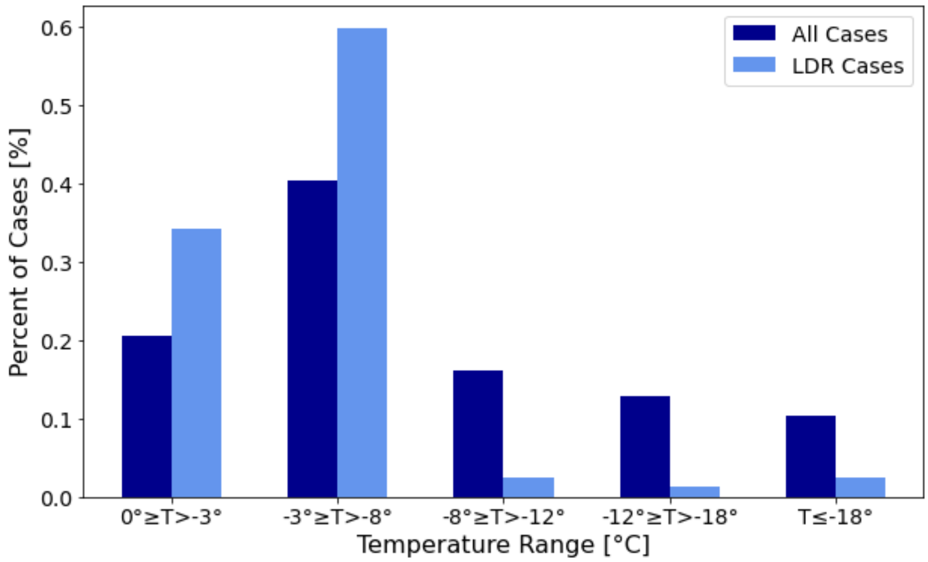

Figure 7: Percentage of verified cases with mean layer temperatures <0°C binned into five temperature categories defined on the x axis. Dark blue bars represent all verified cases with mean layer temperatures <0° C and light blue bars represent only the subset of cases meeting the enhanced LDR thresholds defined in section 4.

5 Selected Cases

5.1 Rime Splintering Temperature Regime (-3 to -8 °C): 15 April 2020

On 15 April 2020, the algorithm detected a long-lived and deep multi-modal layer; the criteria were met from 1000 UTC 15 April through 0100 UTC 16 April. The detected mode had a mean height of 1.07 km and depth of 0.81 km. Over the 14-hour duration of this case, there was substantial variability in the reflectivity, downward velocities, and number of modes, including some periods featuring tri-modal spectra. For illustrative purposes, we narrow in on the hour of 2100-2200 UTC, and examine instantaneous spectra and flags associated with the 10-minute periods surrounding each time (Fig. 8). The flags resulting from the detection algorithm generally align well with the multi-modal layers. Each 10-minute period contains 61 to 142 flags; even if only sustained for 20 minutes, such flag counts would meet the 100 flags necessary for progression through the analysis methodology. At 2200 UTC, the mean detected layer temperature was -4.13 °C: this falls within the temperature range for

https://doi.org/10.5194/egusphere-2025-672
Preprint. Discussion started: 24 February 2025

Hallett-Mossop ice splintering to be possible. Thus, we need to be aware of signals consistent with columnar ice crystals, such as increased LDR. 315

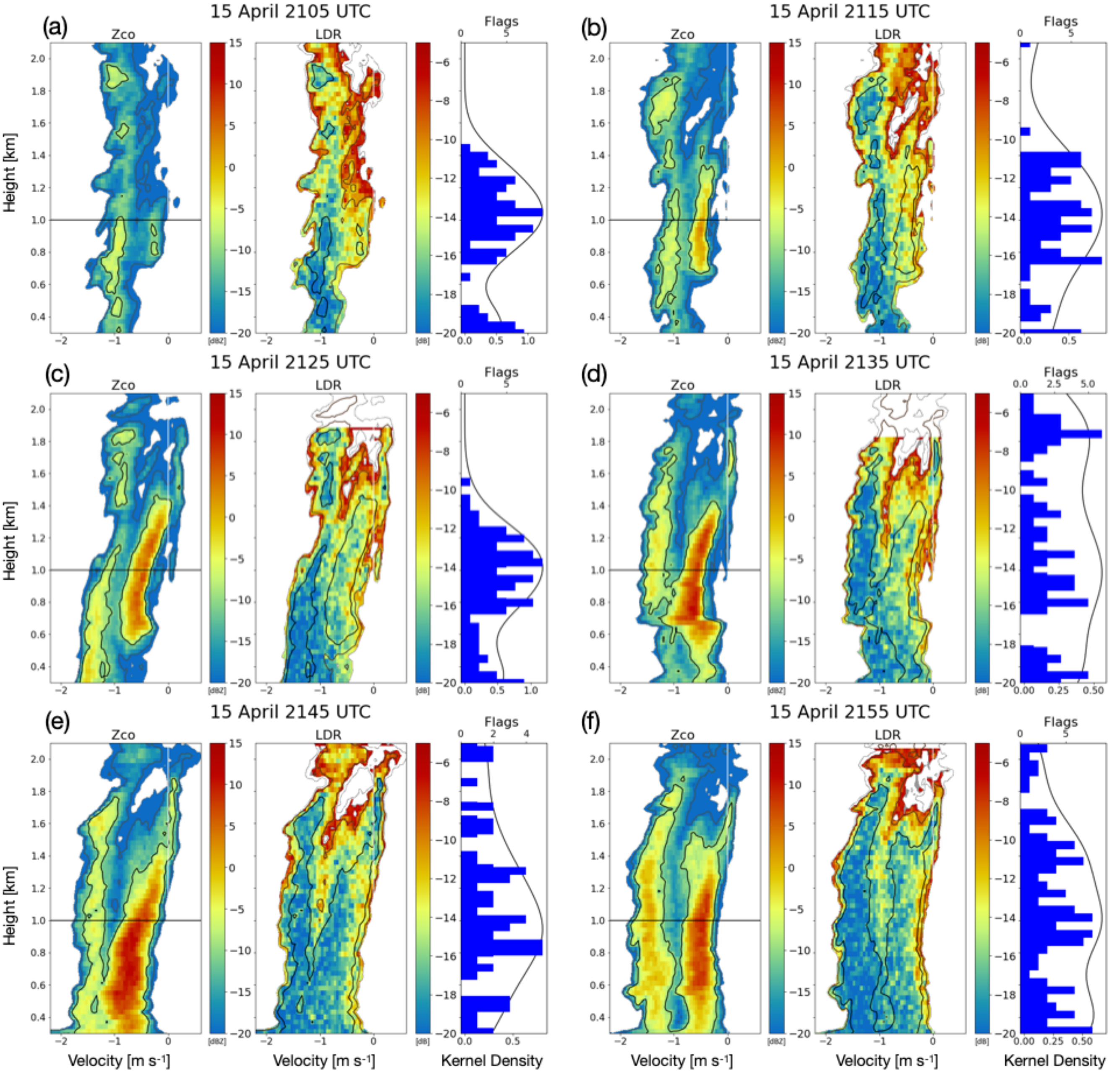

Figure 8: Example case of multi-modal spectra occurring in the temperature range that permits Hallett-Mossop rime splintering. Data are averaged from 10-minute periods centered on (a) 2105 UTC, (b) 2115 UTC, (c) 2125 UTC, (d) 2135 UTC, (e) 2145 UTC, (f) 2155 UTC.from 15 April 2020. Within each sub-panel, we show (left) waterfall plots of spectral co-polar reflectivity Z_{CO}, (middle) waterfall plots of spectral LDR, and (iii) flags detected (blue bars) and a gaussian kernel density estimate of the distribution of flags with height (black line) are plotted. The black contours on the Z_{CO} and LDR panels denote Z_{CO} values > -10 320

dBZ, dark grey contours represent -20 dBZ. Z_{CO} > -25 dBZ are masked out. The black horizontal lines in the Z_{CO} panels show the height at which spectrograms are taken to analyze the modes (Fig. 9).

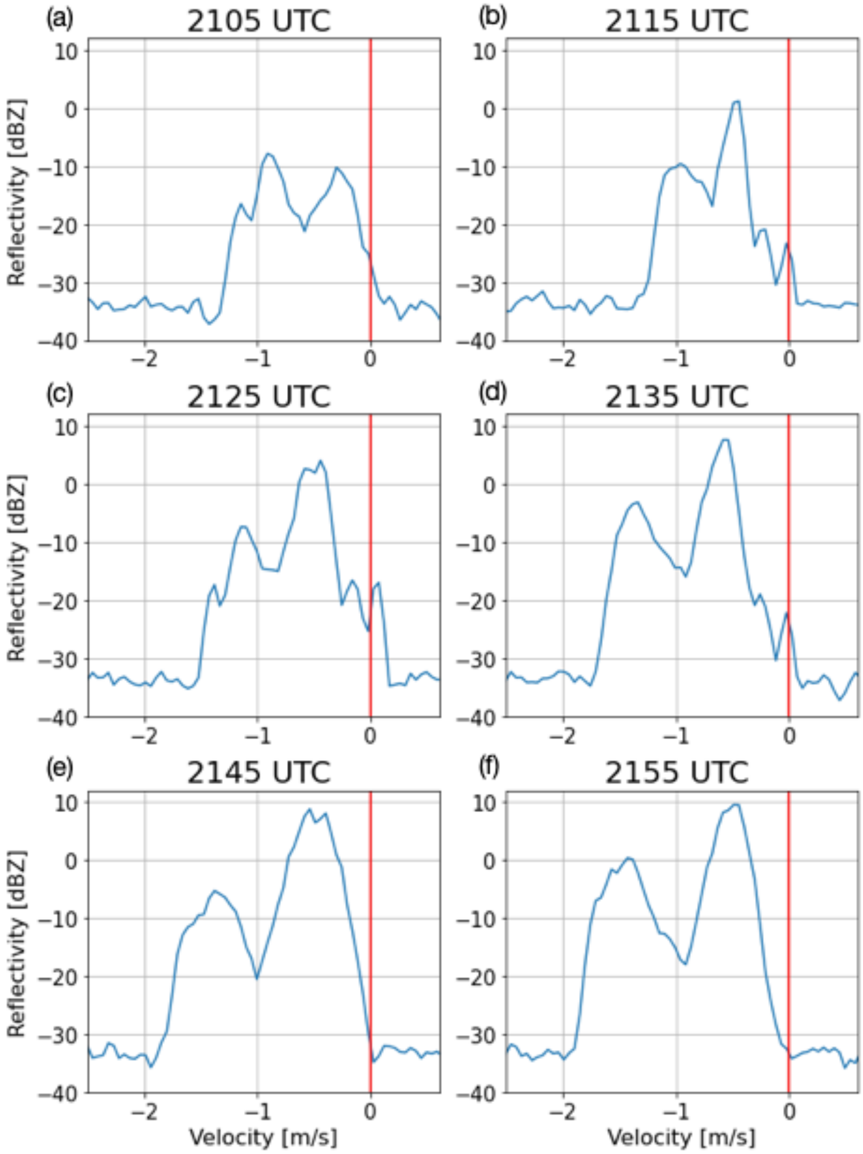

325

Figure 9: Spectrograms taken at 1 km AGL (denoted by the black lines in Figure 8) at (a) 2105 UTC, (b) 2115 UTC, (c) 2125 UTC, (d) 2135 UTC, (e) 2145 UTC, (f) 2155 UTC.

330 At 2105 UTC (Fig. 8a), the spectral reflectivity of both the primary and secondary modes are of a similar magnitude (~ -10 dBZ; Fig. 9a). The slow-falling secondary mode increases in spectral reflectivity to +10 dBZ over the next 40 minutes (Figs. 8b-f, 9b-f), whereas the faster-falling primary mode's spectral reflectivity varies from –5 to 5 dBZ over the hour-long period (Figs. 8a-f; 9a-f). The size (or density) of the observed scatterers likely increases somewhat over the hour, as inferred from the

secondary mode's downward velocity increasing from 0.25 to 0.5 m s^{-1} in the first 10 minutes (Fig. 9a-b), after which it remains generally constant for the rest of the hour (Fig. 9c-f). These fall speeds are consistent with small hydrometeors such as ice crystals or small droplets. The large increase in spectral reflectivity coupled with the comparatively smaller changes in velocity of the slow-falling mode therefore suggests a rapid increase in the number concentration of the scatterers present, along with some growth in the particles' mass. The faster-falling mode's mean velocity increases from 1 to 1.5 m s^{-1} over the hour (Fig. 9); these values suggest it could be snow aggregates or small graupel (e.g., Lamb and Verlinde, 2011; Jensen and Harrington, 2015; Heymsfield et al., 2018). Graupel would indicate that riming is present within this case; riming and graupel are required ingredients for rime splintering.

To understand the make-up of both the slower and faster falling modes, we consult the spectral LDR. At 2115 UTC, a majority of the slower-falling mode has LDR values near -14 dB, which is consistent with columnar ice crystals (e.g., Oue et al., 2015). At the same time, the faster-falling mode has LDR values near -20 dB, approaching KAZR's lower limit. These differences in LDR values between the two modes persist over the hour shown. As the slower-falling mode's spectral reflectivity increases over time, larger LDR values are maintained at higher altitudes and on the slower-falling side (i.e., right edge) of this mode, whereas portions of the mode closer to the surface and closer to the faster falling mode exhibit lower LDR values closer to that of the faster-falling mode. This is likely a result of the ice crystals experiencing processes such as aggregation and riming as they descend.

3.2 Warm Temperature Regime: 3 September 2020

A long-lived multi-modal profile was detected on 3 September 2020 from 16 UTC – 3 UTC the following day. During this event, the profile warmed over time: during the first eight hours, the layer had a mean temperature of -5 °C, but by 0000 UTC 4 September, the layer-average temperature increased to +0.25 °C as determined from the ERA-5 data. To narrow our focus onto a case fitting the "warm" category established in section 4, we examine this multi-modal profile at 2345 UTC when the temperature of the layer was near 0º C (Fig. 10).

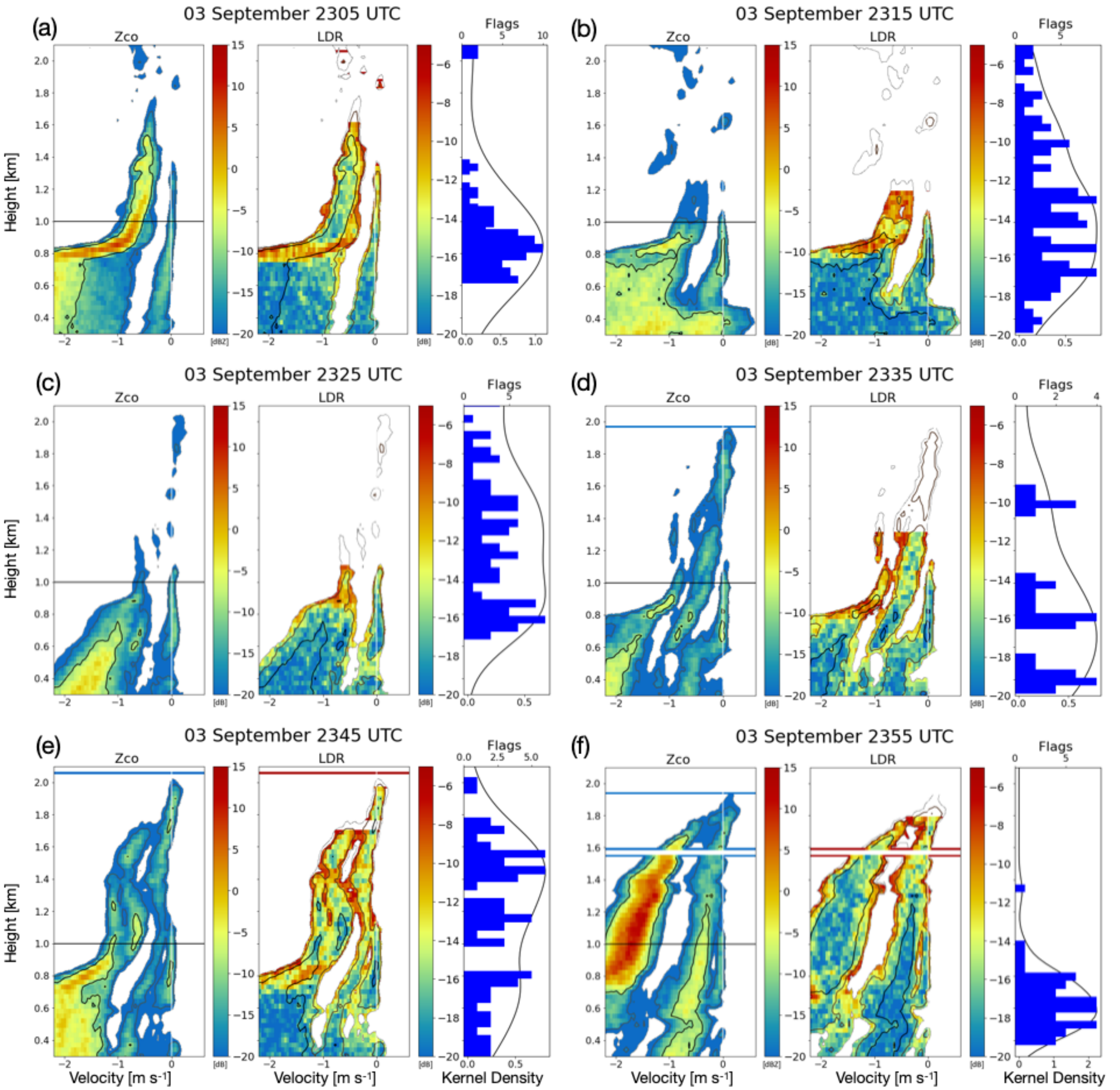

Figure 10: As in Figure 8, for 3 September 2020 at (a) 2305 UTC, (b) 2315 UTC, (c) 2325 UTC, (d) 2335 UTC, (e) 2345 UTC, (f) 2355 UTC.

360

https://doi.org/10.5194/egusphere-2025-672
Preprint. Discussion started: 24 February 2025

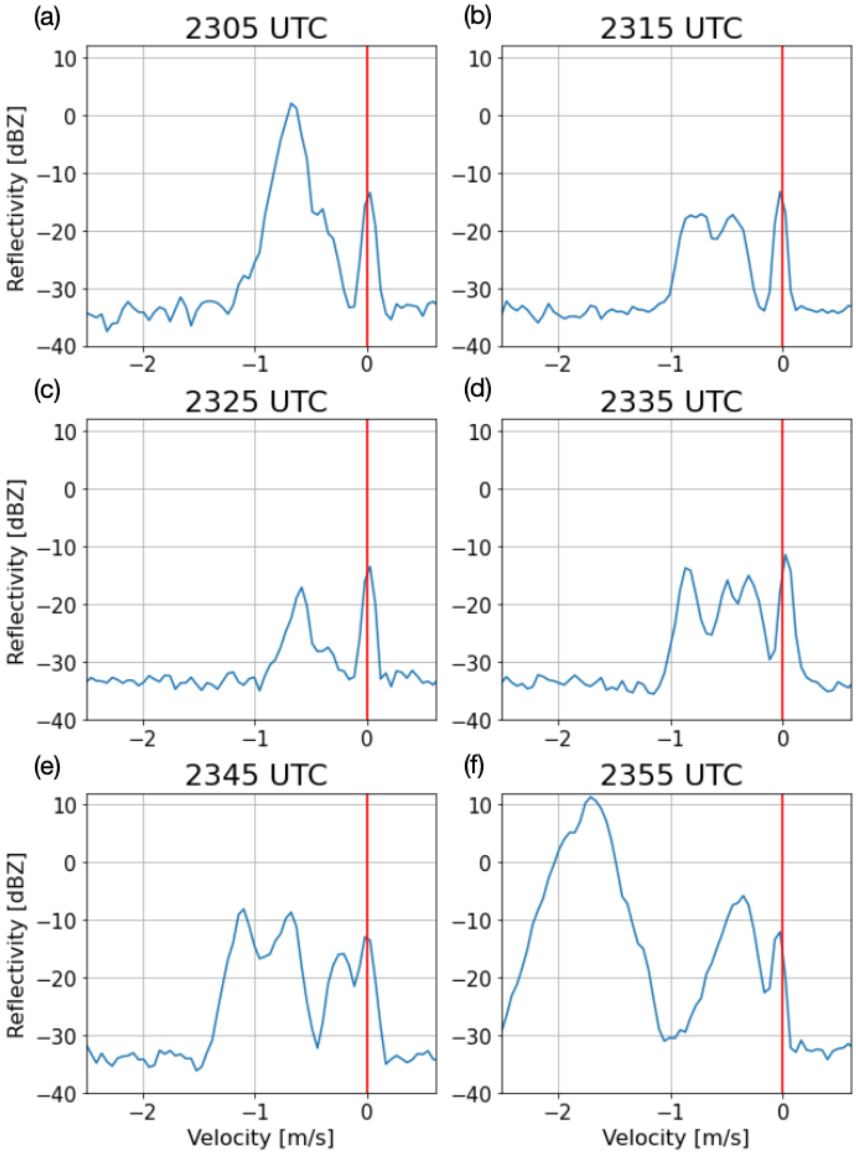

Figure 11: As in Figure 9, for 3 September 2020 at (a) 2305 UTC, (b) 2315 UTC, (c) 2325 UTC, (d) 2335 UTC, (e) 2345 UTC, (f) 2355 UTC.

365 Across the hour shown in Fig. 10, the multi-modal layers are well co-located with the heights where flags were identified by detection algorithm. The heights of these layers vary throughout the hour, especially the low-reflectivity (~ -20 dBZ) modes at 2315-2325 UTC located above 1.3 km (Fig. 10b-d). By 2335 UTC, these become connected to the lower-altitude modes (Fig. 10d). For the purposes of this analysis, we will focus on the modes with spectral reflectivity values exceeding -10 dBZ.

The melting layer is just above 0.8 km, apparent from the increase in reflectivity and the rapid increase in magnitude and 370 broadening of distribution of velocities (the dynamic range of raindrop velocities is nearly an order of magnitude greater than those of snow and ice; e.g., Lamb and Verlinde 2011). Note that the secondary mode persists below the melting layer; despite the faster-falling mode's downward motion exceeding 2 m s^{-1}, the secondary mode is still detected by the flag criteria because the combined (reflectivity-weighted) MDV was still < 2 m s^{-1}. This is most apparent in the snapshot at 2355 UTC (Fig. 10f) in which the secondary mode reflectivity exceeds 5 dBZ, allowing it to contribute enough to the moment variables to result in a MDV that does not exceed the rain filter criteria. This is contrasted with 2305 and 2325 UTC, where the secondary mode below the melting layer has a much weaker reflectivity and no secondary modes are flagged.

The evolution of the reflectivity and velocity of each mode is more easily quantified when examining spectrograms for this case taken at 1 km ARL (Fig. 11). At 2305 UTC, the spectrum is distinctly bi-modal, with an additional indistinct peak on the slow-falling side of the primary mode. At all later times this hour, the spectra maintain three to four peaks. All times shown have the slowest-falling peak centered at ~0 m s^{-1}. This is consistent with cloud droplets and/or particles suspended in an updraft.

From 2335 to 2345 UTC, the observed spectral reflectivity exhibits a quad-modal distribution (Fig. 10d, 11d). Beginning at 2335, the left edge of the fastest-falling mode broadens and shifts towards greater fall speeds. Although radar data alone are insufficient to determine the process(es) leading to the four distinct modes during this period, the end result is a significantly stronger primary mode at 2355 UTC with spectral reflectivity values ~10 dBZ, much greater than 10 minutes prior (Fig. 10f, 11f).

Generally, the slower-falling modes in this case have relatively low spectral reflectivity (-10 to -5 dBZ); thus, because of the weak signal, LDR is positively biased and less reliable, making it more difficult to determine if the modes are caused by ice or liquid. Signals greater than -10-dBZ are more likely to be reliable than those signals associated with weaker returns. Thus, any LDR increase associated with Z decreasing to values below -10 dBZ are assumed to be biased and thus not used in the interpretation. However, at 2355 (Fig. 10f, 11f), when the secondary mode spectral reflectivity values exceed -10 dBZ over a 1-km depth, there is no enhancement of LDR and thus no associated depolarization signals to suggest that this mode contains ice. Rather, it is likely that this mode is composed of liquid droplets, likely drizzle drops due to the small fall speeds of 0 to 1 m s^{-1}. The melting mode near 0.9 km has the greatest spectral reflectivity values observed in this case and is collocated with an enhancement of LDR. The slower-falling modes, for example at 2345 UTC, are weaker, with spectral reflectivities < -10 dBZ, and thus we cannot infer their composition.

4.3 Dendritic Growth Temperature Regime: 4 January 2022

The detected case on 4 January 2022 lasted four hours from 1300 UTC to 1700 UTC. This event had an average mean layer temperature of –14 °C, much colder than the two cases previously discussed and consistent with the dendritic growth layer (e.g., Lamb and Verlinde, 2011). Only a shallow multi-modal layer was detected by the criterion of minimum of 5 dB difference from the primary mode (Fig. 12). The distinct layer is seen most clearly when looking at the 0-dBZ contour (Fig. 12) or the spectrograms taken at 2.5 and 3.0 km (Fig. 13). At 2.5 km, a secondary mode is still detected at all times shown, as indicated by the 10-minute flag counts (Fig. 12, right-most subpanels). However, the instantaneous spectra are more variable, with the secondary mode appearing less distinct at 1330 and 1340 UTC (Fig. 13b, d) and nonexistent at 1335 UTC (Fig. 13c). This illustrates the sensitivity of the detection algorithm to identify a secondary mode in a quickly changing radar presentation.

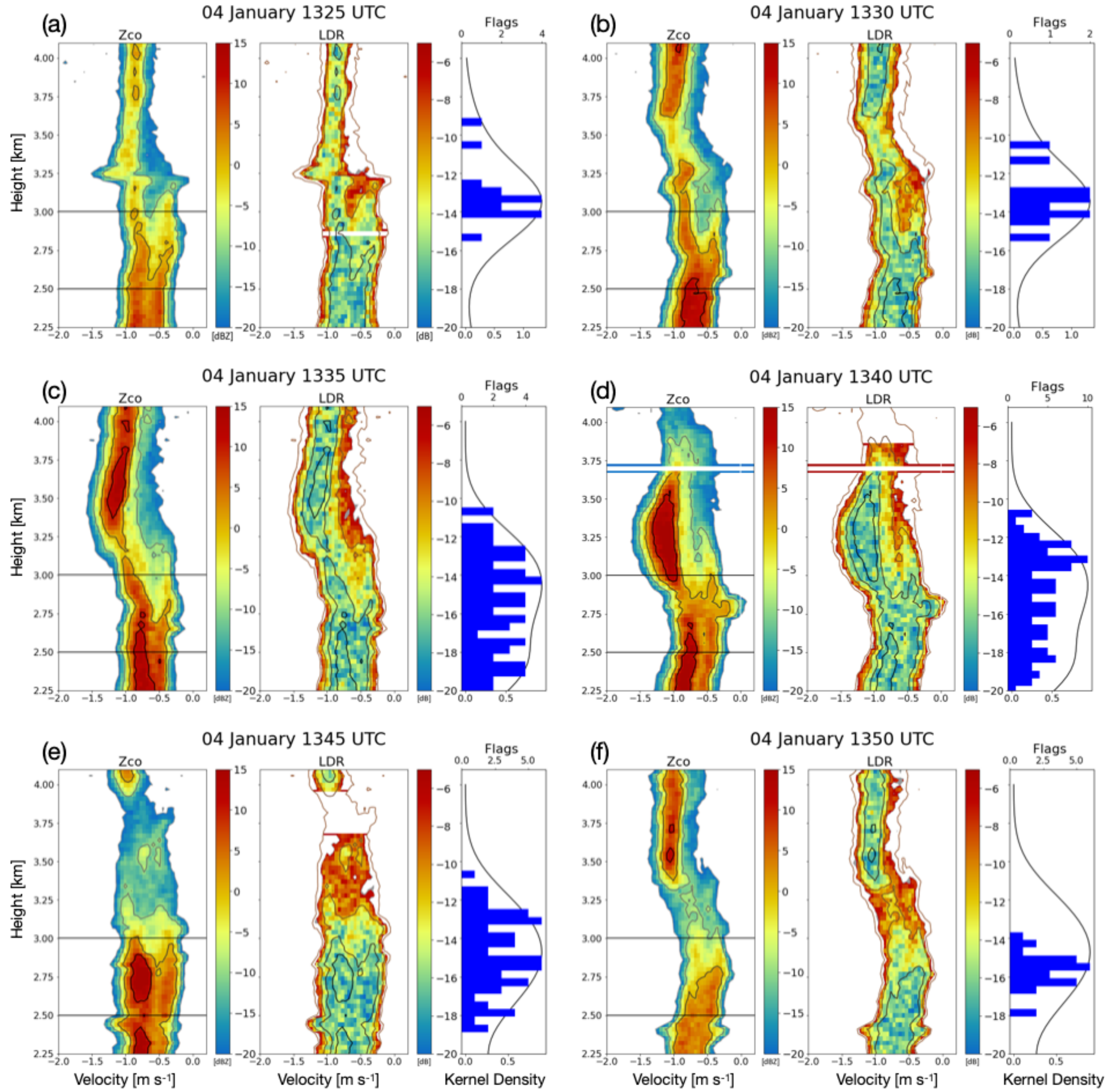

Figure 12: As in Figure 8, with spectrograms taken at 2.5 and 3.0 km, for 4 January 2022 at (a) 1325 UTC, (b) 1330 UTC, (c) 1335 UTC, (d) 1340 UTC, (e) 1345 UTC, (f) 1350 UTC.

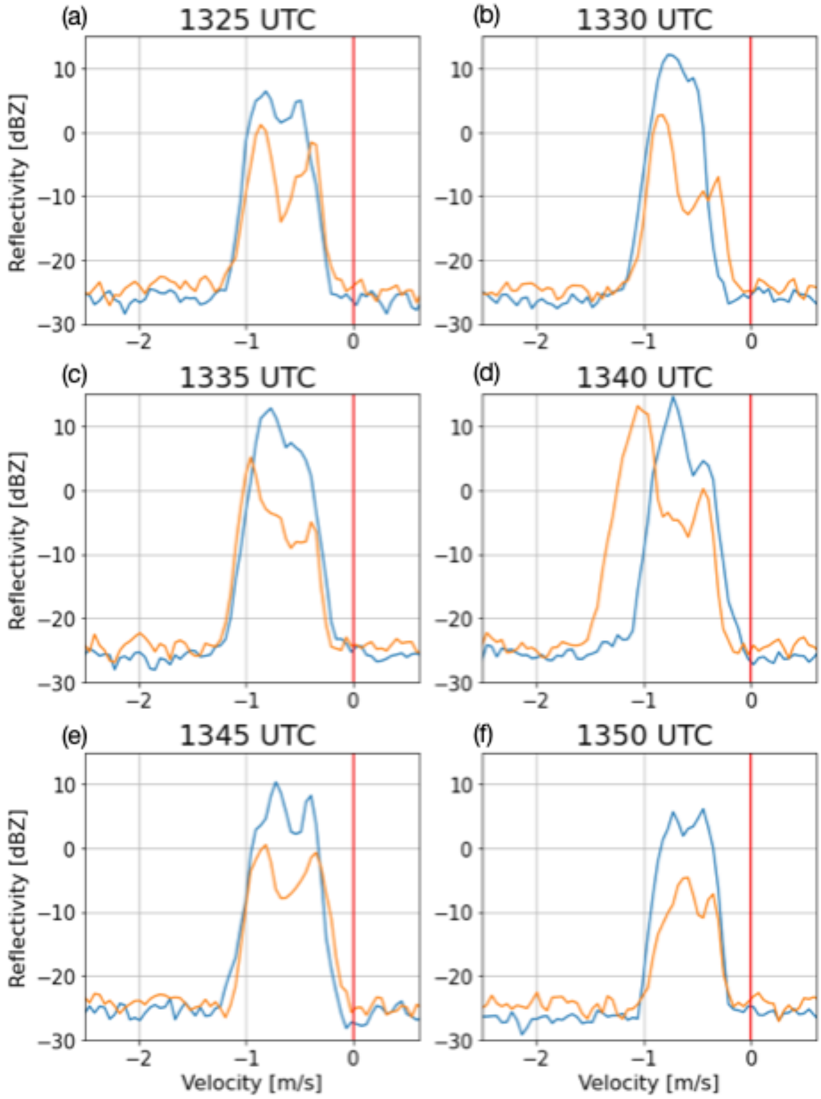

Figure 13: As in Figure 9, with spectrograms taken at 2.5 (blue) and 3.0 (orange) km, for 4 January 2022 at (a) 1325 UTC, (b) 1330 UTC, (c) 1335 UTC, (d) 1340 UTC, (e) 1345 UTC, (f) 1350 UTC.

The two modes in this case exhibit more similar velocities than those in the previous two cases: the primary mode varies from being centered on 0.8 to 1.0 m s^{-1} while the secondary mode sits at about 0.5 m s^{-1}. These fall speeds can be explained by a range of hydrometeor types, but small and/or less-dense snow aggregates are likely in the primary mode, especially given this layer having a temperature characteristic of the dendritic growth zone. The secondary mode may be explained by "early" aggregates (Moisseev et al., 2015) or pristine crystals (e.g., Lamb and Verlinde 2011). Early aggregates are consistent with how the secondary mode extends towards the primary mode as it approaches the surface, similar to how an early aggregate may collect other crystals and increase its mass, and consequently, its fall speed. Throughout this case, there is no clear enhancement in LDR for either mode that would be consistent with pristine columns or other ice crystals or crystal fragments with mass distributed asymmetrically in the horizontal plane. Thus, we speculate the multi-modal spectra arise from primary nucleation of planar crystals and their subsequent aggregation, in the presence of smaller aggregates falling into the layer from further aloft.

6 Conclusions

Following a three-year test of the multi-modal spectra detection algorithm described in Part 1, we found that it was 90.8% successful in identifying cases with secondary (and, at times, tertiary) modes. Using this moment-based detection algorithm will save users time and computational expenses of processing large spectral datasets. Users looking for case studies of processes associated with multi-modal spectra, particularly those associated with mixed-phase or secondary ice production processes, can use this to identify dates and times of interest, narrowing down the number and size of radar spectra files needed. There may be merits to running this algorithm for long-term vertically pointing Ka-band radar datasets (e.g., the KAZR at DOE ARM sites) so that users can quickly identify these periods of interest.

To further refine the criteria and explore potential processes associated with these modes, an LDR flag can facilitate finding cases specific to ice or drizzle events. Although moment-based LDR criteria need to be accompanied by spectral LDR analysis to confirm the findings, the detection criteria can be helpful in narrowing down the pool of potential events. In the LDR analysis, we showed that nearly 60% cases meeting the criteria for having enhanced LDR were found in layers with temperatures commonly associated with both columnar ice crystal growth and H-M rime splintering (-8 to - 3 °C). Users interested in pursuing mixed-phase or secondary ice processes can use this as a springboard for further, in-depth analyses on LDR-flagged cases, that can potentially confirm any processes active within the identified events. There are variable LDR limits for different radars, so further application of this approach to flagging enhanced LDR regions should keep in mind the potential variations in observed LDR by different instruments. Our approach to identify events with an hourly mean LDR that was two standard deviations greater than the annual mean can be easily adapted to future studies with other radars.

Detected cases of multi-modal spectra within three temperature categories were examined: warm/near melting (> -3°C), Hallett-Mossop (-8 to -3°C), and dendritic growth zone (-12 to -8°C). In all three cases, the algorithm detected flags that aligned with the multi-modal layers. The warm case demonstrated that a bi-modal layer below the melting layer can still be detected using the algorithm, even with the rain filter. The three cases also illustrated that the detection is not limited to bi-modality, but that the algorithm will also identify layers that contain greater than two distinct modes.

While useful, radar alone is often insufficient to make concrete determinations of active processes. Application of this multi-modal spectra detection algorithm and LDR analysis benefits from accompanied analysis of atmospheric temperature profiles. Users can incorporate analyses of observational or reanalysis datasets to better understand what processes may be active in any detected multi-modal cases. Through LDR and temperature analysis, one may speculate about the active processes, but more in-depth process attribution is better supported by in-situ observations and particle imagery capable of confirming the

https://doi.org/10.5194/egusphere-2025-672
Preprint. Discussion started: 24 February 2025

presence, size, and concentrations of ice crystals, when available. Overall, this study has demonstrated the utility in identifying cases with processes capable of producing bi-, tri-, and quad-modal spectra via automation, which can be used to leverage large, archived radar data sets for new projects.

Appendix

As discussed in section 3, the temporal variation of flag counts is visualized in Fig. A1 and A2. Note that in 2022, the months of July through September include periods of missing data (5-18 days) containing no flags. The periods of missing data in Fig. A1 are apparent because in 2020 and 2023 these are some of the months with the higher flag counts and more long duration events. 2023, visualized in Fig. A2, shows more flag activity spread across all months than the previous years. Note that in 2023, July is excluded due to having missing spectra data from July 3-23; moment data is available so flag counts are still depicted in Fig. A2. While containing almost the same number of verified cases as 2020 (2023 has one fewer), 2020 had approximately one third of its cases occurring in September. In contrast, in 2023 three months had greater than 10 detected cases (August, September, and October). The examination of the frequency and seasonality of these events over the three year period, while providing a valuable perspective, are taken over a relatively short period for conclusive findings on the seasonality of multi-modal spectra events at the NSA site.

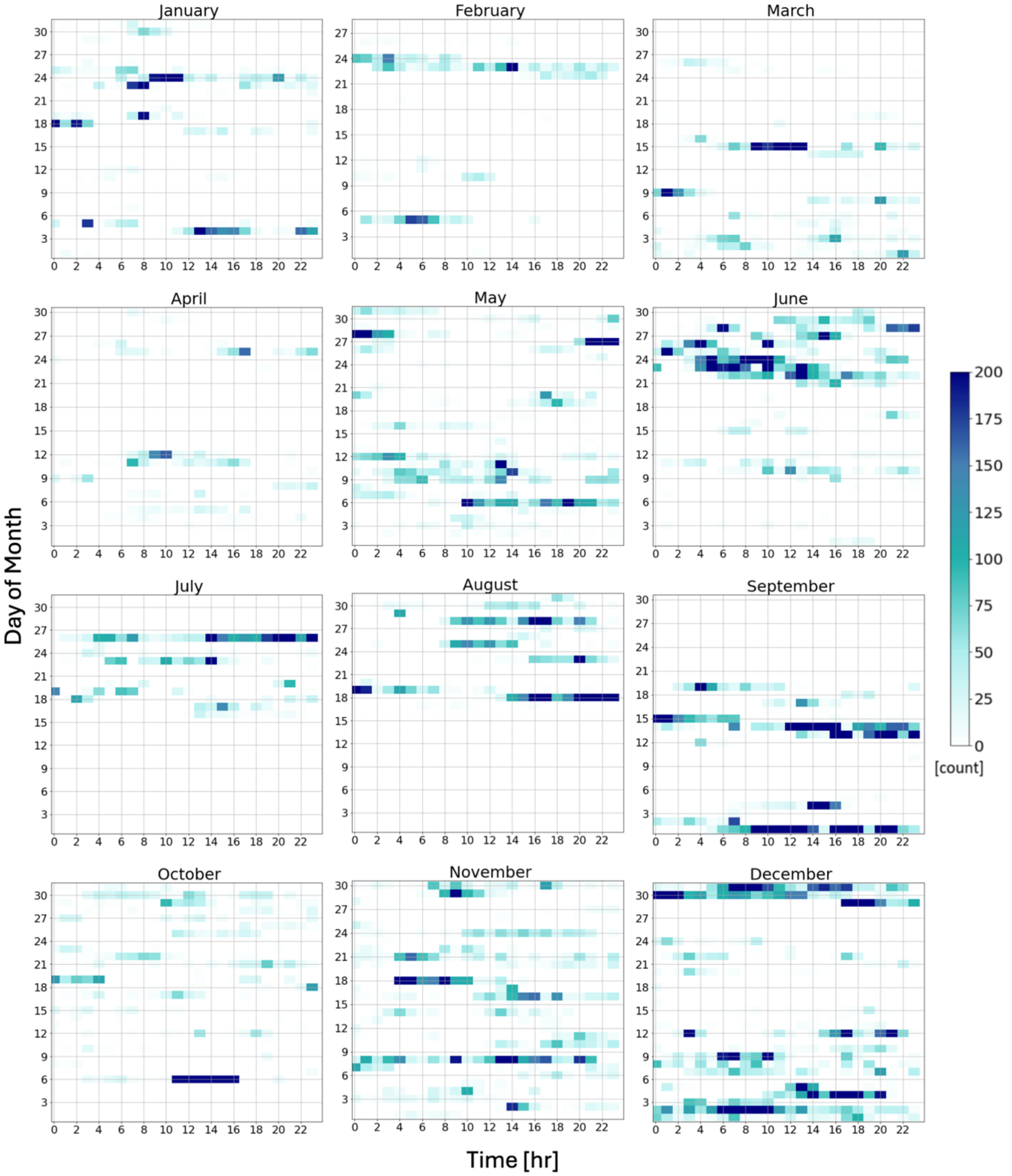

470 **Figure A1: As in Figure 4, but for 2022.**

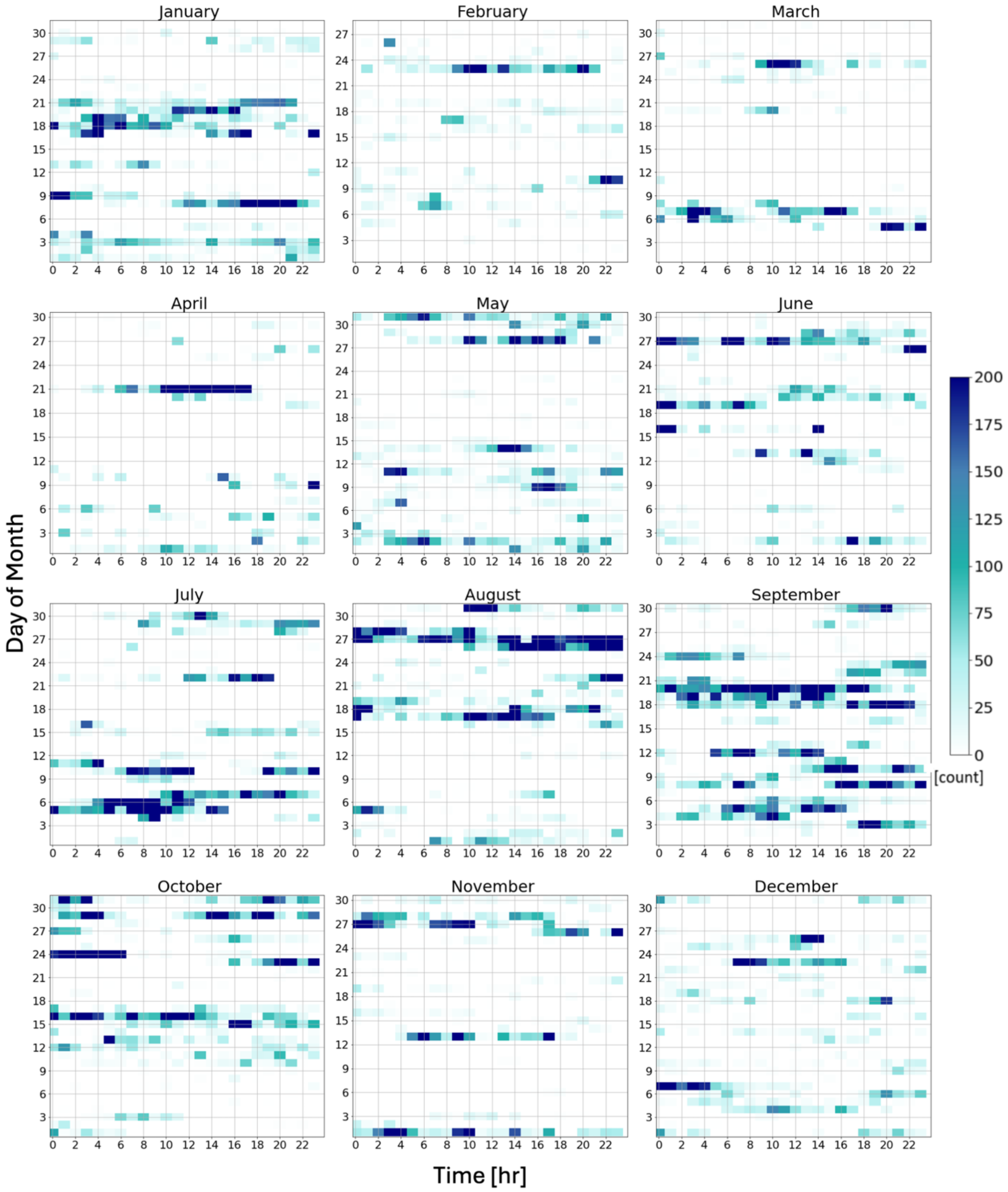

Figure A2: As in Figure 4, but for 2023. Results from July 2023 are displayed because vertically pointing moment data was available, but note that the spectra from this month was not available for verification.

Code and Data Availability

KAZR moment and spectra data are available online at https://adc.arm.gov/discovery. ERA-5 reanalysis data is available online through the ECMWF Climate Data Store at https://cds.climate.copernicus.eu/.

Author Contributions

This work stems from the dissertation work of SW, advised and guided by MRK.

Competing interests

The contact author has declared that none of the authors has any competing interests.

Acknowledgments

Support for SW and MRK comes from the U.S. Department of Energy Atmospheric System Research program Grant DE-SC0018933, the NASA Earth Venture Suborbital-3 (EVS-3) program under Grant 80NSSC19K0452, and academic appointments at The Pennsylvania State University. Data were obtained from the Atmospheric Radiation Measurement (ARM) Program sponsored by the U.S. Department of Energy, Office of Science, Office of Biological and Environmental Research, Climate and Environmental Sciences Division. We are grateful for the DOE ARM program's continued support of the KAZR facilities, data processing, and data storage that made this study possible. We would also like the thank Edward Luke for his helpful discussions about LDR and radar spectra.

References

Atmospheric Radiation Measurement (ARM) user facility. 2019. Ka ARM Zenith Radar (KAZRCFRSPCGECOPOL), 2020-01-01 to 2023-12-31, North Slope Alaska (NSA) Central Facility, Barrow AK (C1). Compiled by Y. Feng, I. Lindenmaier, K. Johnson, A. Matthews, T. Wendler, V. Melo de Castro, M. Deng and M. Rocque. ARM Data Center.

Billault-Roux, A.-C., Georgakaki, P., Gehring, J., Jaffeux, L., Schwarzenboeck, A., Coutris, P., Nenes, A., & Berne, A. (2023). Distinct secondary ice production processes observed in radar Doppler spectra: Insights from a case study. *EGUsphere*, *2023*, 1–40. https://doi.org/10.5194/egusphere-2023-478

Devisetty, H., Jha, A., Das, S., Deshpande, S., Krishna, M., Kalekar, P., & Pandithurai, G. (2019). A case study on bright band transition from very light to heavy rain using simultaneous observations of collocated X-and Ka-band radars. *Journal of Earth System Science*, *128*. https://doi.org/10.1007/s12040-019-1171-0

Feng, Y.-C., Bharadwaj, N., Lindenmaier, I., Johnson, K., Nelson, D., Isom, B., Hardin, J., Matthews, A., Wendler, T., Melo de Castro, V., & al, et. (n.d.-a). Ka ARM Zenith Radar (KAZRCFRSPCGECOPOL), 2019-06-10 to 2025-01-27, North Slope Alaska (NSA), Central Facility, Barrow AK (C1). In *Atmospheric Radiation Measurement (ARM) user facility*. https://doi.org/10.5439/1608603

Feng, Y.-C., Bharadwaj, N., Lindenmaier, I., Johnson, K., Nelson, D., Isom, B., Hardin, J., Matthews, A., Wendler, T., Melo de Castro, V., & al, et. (n.d.-b). Ka ARM Zenith Radar (KAZRCFRSPCGEXPOL), 2019-06-10 to 2025-01-27, North Slope Alaska (NSA), Central Facility, Barrow AK (C1). In *Atmospheric Radiation Measurement (ARM) user facility*. https://doi.org/10.5439/1608590

Field, P. R., Lawson, R. P., Brown, P. R. A., Lloyd, G., Westbrook, C., Moisseev, D., Miltenberger, A., Nenes, A., Blyth, A., Choularton, T., Connolly, P., Buehl, J., Crosier, J., Cui, Z., Dearden, C., DeMott, P., Flossmann, A., Heymsfield, A., Huang, Y., … Sullivan, S. (2017). Secondary Ice Production: Current State of the Science and Recommendations for the Future. *Meteorological Monographs*, *58*(1), 7.1-7.20. https://doi.org/10.1175/AMSMONOGRAPHS-D-16-0014.1

Forbes, R., Tompkins, A. M., & Untch, A. (2011, September). A new prognostic bulk microphysics scheme for the IFS. In *ECMWF Technical Memoranda* (Issue 649, p. 22). ECMWF. https://doi.org/10.21957/bf6vjvxk

Hallett, J., & Mossop, S. C. (1974). Production of secondary ice particles during the riming process. *Nature*, *249*(5452), 26–28. https://doi.org/10.1038/249026a0

Hersbach, H., Bell, B., Berrisford, P., Biavati, G., Horányi, A., Muñoz Sabater, J., Nicolas, J., Peubey, C., Radu, R., Rozum, I., Schepers, D., Simmons, A., Soci, C., Dee, D., & Thépaut, J.-N. (2023). *ERA5 hourly data on pressure levels from 1940 to present*. Copernicus Climate Change Service (C3S) Climate Data Store (CDS). https://doi.org/10.24381/cds.bd0915c6

Hersbach, H., Bell, W., Berrisford, P., Horányi, A., J, M.-S., Nicolas, J., Radu, R., Schepers, D., Simmons, A., Soci, C., & Dee, D. (2019, April). Global reanalysis: Goodbye ERA-Interim, hello ERA5. In *ECMWF Newsletter* (pp. 17–24). https://doi.org/10.21957/vf291hehd7

Heymsfield, A., Szakáll, M., Jost, A., Giammanco, I., & Wright, R. (2018). A Comprehensive Observational Study of Graupel and Hail Terminal Velocity, Mass Flux, and Kinetic Energy. *Journal of the Atmospheric Sciences*, *75*(11), 3861–3885. https://doi.org/10.1175/JAS-D-18-0035.1

Jensen, A. A., & Harrington, J. Y. (2015). Modeling Ice Crystal Aspect Ratio Evolution during Riming: A Single-Particle Growth Model. *Journal of the Atmospheric Sciences*, *72*(7), 2569–2590. https://doi.org/10.1175/JAS-D-14-0297.1

Korolev, A., McFarquhar, G., Field, P. R., Franklin, C., Lawson, P., Wang, Z., Williams, E., Abel, S. J., Axisa, D., Borrmann, S., Crosier, J., Fugal, J., Krämer, M., Lohmann, U., Schlenczek, O., Schnaiter, M., & Wendisch, M. (2017). Mixed-Phase Clouds: Progress and Challenges. *Meteorological Monographs*, *58*, 5.1-5.50. https://doi.org/10.1175/AMSMONOGRAPHS-D-17-0001.1

Kumjian, M. R., Prat, O. P., Reimel, K. J., van Lier-Walqui, M., & Morrison, H. C. (2022). Dual-Polarization Radar Fingerprints of Precipitation Physics: A Review. *Remote Sensing*, *14*(15), Article 15. https://doi.org/10.3390/rs14153706

Kumjian, M. R., Tobin, D. M., Oue, M., & Kollias, P. (2020). Microphysical Insights into Ice Pellet Formation Revealed by Fully Polarimetric Ka-Band Doppler Radar. *Journal of Applied Meteorology and Climatology*, *59*(10), 1557–1580. https://doi.org/10.1175/JAMC-D-20-0054.1

Lamb, D., & Verlinde, J. (2011). *Physics and Chemistry of Clouds*. Cambridge University Press. https://doi.org/10.1017/CBO9780511976377

Luke, E. P., Kollias, P., & Shupe, M. D. (2010). Detection of supercooled liquid in mixed-phase clouds using radar Doppler spectra. *Journal of Geophysical Research: Atmospheres*, *115*(D19). https://doi.org/10.1029/2009JD012884

Luke, E. P., Yang, F., Kollias, P., Vogelmann, A. M., & Maahn, M. (2021). New insights into ice multiplication using remote-sensing observations of slightly supercooled mixed-phase clouds in the Arctic. *Proceedings of the National Academy of Sciences*, *118*(13), e2021387118. https://doi.org/10.1073/pnas.2021387118

Moisseev, D. N., Lautaportti, S., Tyynela, J., & Lim, S. (2015). Dual-polarization radar signatures in snowstorms: Role of snowflake aggregation. *Journal of Geophysical Research: Atmospheres*, *120*(24), 12644–12655. https://doi.org/10.1002/2015JD023884

Morrison, H., de Boer, G., Feingold, G., Harrington, J., Shupe, M. D., & Sulia, K. (2012). Resilience of persistent Arctic mixed-phase clouds. *Nature Geoscience*, *5*(1), 11–17. https://doi.org/10.1038/ngeo1332

Oue, M., Kumjian, M. R., Lu, Y., Verlinde, J., Aydin, K., & Clothiaux, E. E. (2015). Linear Depolarization Ratios of Columnar Ice Crystals in a Deep Precipitating System over the Arctic Observed by Zenith-Pointing Ka-Band Doppler Radar. *Journal of Applied Meteorology and Climatology*, *54*(5), 1060–1068. https://doi.org/10.1175/JAMC-D-15-0012.1

Shupe, M. D., & Intrieri, J. M. (2004). Cloud Radiative Forcing of the Arctic Surface: The Influence of Cloud Properties, Surface Albedo, and Solar Zenith Angle. *Journal of Climate*, *17*(3), 616–628. https://doi.org/10.1175/1520-0442(2004)017<0616:CRFOTA>2.0.CO;2

Shupe, M. D., Walden, V. P., Eloranta, E., Uttal, T., Campbell, J. R., Starkweather, S. M., & Shiobara, M. (2011). Clouds at Arctic Atmospheric Observatories. Part I: Occurrence and Macrophysical Properties. *Journal of Applied Meteorology and Climatology*, *50*(3), 626–644. https://doi.org/10.1175/2010JAMC2467.1

Sinclair, V. A., Moisseev, D., & von Lerber, A. (2016). How dual-polarization radar observations can be used to verify model representation of secondary ice. *Journal of Geophysical Research: Atmospheres*, *121*(18), 10,954-10,970. https://doi.org/10.1002/2016JD025381

Toto, T., & Giangrande, S. (n.d.). Ka-Band ARM Zenith RADAR (KAZR) CF-Radial, Corrected VAP (KAZRCFRCORGE), 2019-10-28 to 2025-02-01, North Slope Alaska (NSA), Central Facility, Barrow AK (C1). In *Atmospheric Radiation Measurement (ARM) user facility*. https://doi.org/10.5439/1560129

Verlinde, J., Rambukkange, M. P., Clothiaux, E. E., McFarquhar, G. M., & Eloranta, E. W. (2013). Arctic multilayered, mixed-phase cloud processes revealed in millimeter-wave cloud radar Doppler spectra. *Journal of Geophysical Research: Atmospheres*, *118*(23), 13,199-13,213. https://doi.org/10.1002/2013JD020183

Wugofski, Sarah, Matthew R. Kumjian, Mariko Oue, and Pavlos Kollias. Detection of Multi-Modal Doppler Spectra. Part 1: Establishing Characteristic Signals in Radar Moment Data. *Submitted to Atmospheric Measurement Techniques,* 2025.

Zuidema, P., Baker, B., Han, Y., Intrieri, J., Key, J., Lawson, P., Matrosov, S., Shupe, M., Stone, R., & Uttal, T. (2005). An Arctic Springtime Mixed-Phase Cloudy Boundary Layer Observed during SHEBA. *Journal of the Atmospheric Sciences*, *62*(1), 160–176. https://doi.org/10.1175/JAS-3368.1